Science of the Total Environment 842 (2022) 156736

Contents lists available at ScienceDirect

Science of the Total Environment

journal homepage: www.elsevier.com/locate/scitotenv

Probabilistic hydro-geomorphological hazard assessment based on UAV-derived high-resolution topographic data: The case of Basento river (Southern Italy)

Marco La Salandra *, Rodolfo Roseto, Daniela Mele, Pierfrancesco Dellino, Domenico Capolongo

Department of Earth and Geoenvironmental Sciences, University of Bari, Italy

HIGHLIGHTS

- Original approach to assess the river hydro-geomorphological hazard by means of UAV-based high-resolution data.
- DEMs resolution, roughness coefficient and morphological change detection sensitivity analyses were performed.
- Results showed significant impact of high-resolution UAV data for the hydro-geomorphological hazard assessment.

GRAPHICAL ABSTRACT

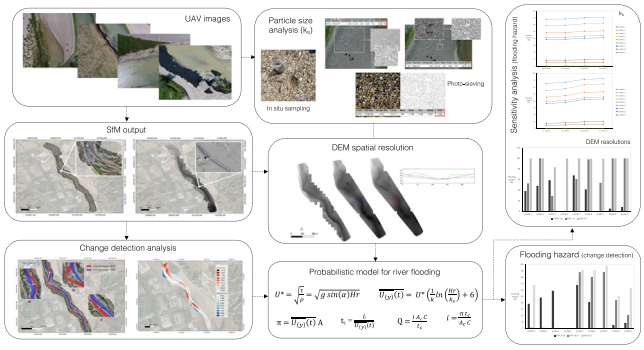

ARTICLE INFO

Editor: Martin Drews

Keywords:
UAV imagery
Structure from motion
Photo-sieving
High-resolution topographic data
Hydro-geomorphological hazard
Fluvial system

ABSTRACT

The combined use of Unmanned Aerial Vehicles (UAVs) and Structure from Motion (SfM) photogrammetry allows the collection and processing of high-resolution data on demand, which is key for the constant and detailed monitoring of the fluvial environment. In addition, through the ever-increasing development of new techniques of mapping and data processing (i.e., UAVs swarm, BVLOS flight missions, high-performance photogrammetry workflow), it is now possible to detect large areas at high-resolution, providing support for spatiotemporal insights into hydro-geomorphological processes and hazard assessment, in order to ensure an effective management and to prevent catastrophic phenomena (i.e., floods).

The main goal of this paper is to use UAV-based high-resolution topographic data to constrain the probabilistic hazard assessment of extended reaches of Basento river (Basilicata, Italy). To demonstrate the influence of geomorphology and riverbed sediment on hazard assessment, a sensitivity analysis was carried out on the resolution of the UAV-derived DEMs; on the riverbed roughness coefficient resulting from photo-sieving analysis and on the morphological change detection over short-time ranges (2019–2021). We found that lower resolution DEMs lead to an increase of flooding probability (in several river cross-sections an increase even higher than 99 % resulted), and that a greater roughness coefficient involves an increase in the probability of flooding (with a maximum increase of about 9 %). Moreover, the multitemporal high-resolution outputs resulting from SfM allowed the identification of morphological changes, in short-times, caused by an anthropic modification of the river bank, which significantly affected the flooding hazard.

* Corresponding author.
E-mail address: marco.lasalandra@uniba.it (M. La Salandra).

http://dx.doi.org/10.1016/j.scitotenv.2022.156736
Received 2 April 2022; Received in revised form 30 May 2022; Accepted 12 June 2022
Available online 16 June 2022

1. Introduction

The use of remote sensing is of an increasing importance for studying fluvial systems and is more often coupled with hydrological and geomorphological modelling (Capolongo et al., 2019).

In fact, for a better hazard assessment, the changes in flow regime that are associated with sudden climate changes require a detailed analysis of the continuous spatiotemporal modifications of the river basin. Accurately capturing and recording hydro-geomorphological basin changes is of key importance, since these processes can be very rapid (Koutalakis et al., 2020) and can result in flood phenomena that determine harmful impacts on facilities, productive activities and, especially, human lives (Neal et al., 2009; Kwak et al., 2013; Rinaldi et al., 2017; Ahamed et al., 2017; Fanta-Jende et al., 2020).

Hydro-geomorphological processes are linked to changes in the landform caused by hydrological and hydraulics processes (Scheidegger, 1973), which include channel form and mobility, continuity and connectivity of the stream, slope angle of the channel, riverbed structure, type and size of the substrate, water depth and flow velocity (De Musso et al., 2020).

Using a high-resolution topographic analysis, a detailed characterization of sediment transport (erosional and depositional processes), channel planform, and spatiotemporal location of the hydro-geomorphological units (Vaughan et al., 2009; Bizzi et al., 2016) can be obtained, which can greatly improve our understanding of fluvial regimes (Horritt and Bates, 2001; Bates et al., 2003; Podhorányi et al., 2013).

Various tools and techniques can be used for such an aim, both ground-based and airborne. Ground-based techniques (series of field surveys supported by topographic instruments such as total station and differential GNSS) ensure high resolution, but the extension of the investigated area is limited due to the high instrumental cost, the reduced portability of instruments and their power requirements (Westoby et al., 2012; Md Ali et al., 2015).

In contrast, airborne and satellite sensors provide a high-range coverage, but are often limited by a coarse spatiotemporal resolution that does not allow a detailed reconstruction of topography (e.g., Endreny et al., 2000; Boulton and Stokes, 2018).

Thanks to the technological advancement of the last decades and the availability of cheap consumer-grade high-resolution digital cameras, the combined use of Unmanned Aerial Vehicles (UAVs) and Structure from Motion photogrammetry (SfM) makes it now possible to address such shortcomings. These modern tools allow on-demand acquisition of high-quality spatial data with high-temporal frequency (Mancini et al., 2013; Micheletti et al., 2015; Manfreda et al., 2018), which are useful to monitor the sudden relief changes that can influence flood inception (Niethammer et al., 2012; Tamminga et al., 2015; Rusnák et al., 2018; Karamuz et al., 2020).

Structure from Motion is a photogrammetric range imaging technique for estimating 3D information through overlapping 2D images (Eltner and Sofia, 2020). SfM represents also an advanced tool for studying fluvial hydrogeomorphology (e.g., Thumser et al., 2017; Hemmelder et al., 2018). It can be applied to a wide range of temporal and spatial scales, and resolutions up to an unprecedented level of detail, e.g., for producing multitemporal topographic models of riverine environments (Fonstad et al., 2013) and detecting morphological changes (Klein et al., 2007; Wheaton et al., 2010; Marteau et al., 2017).

The duration of UAV flight times possible nowadays (Jung et al., 2019; Jain et al., 2020) allows for Beyond Visual Line Of Sight (BVLOS) flight missions (Davies et al., 2018; Fang et al., 2018). They can overcome the "close-range" limit, making it possible to collect large datasets that feed high-performance computing photogrammetric workflows (La Salandra et al., 2021), thereby greatly increasing the spatial resolution of the topographic models derived from SfM.

In these workflows, the primary baseline of ground topography is represented by Digital Elevation Models (DEMs), which resolution needs to be optimized to the scale of the specific hydro-geomorphological parameters of interest, which span over a very wide range down to centimeters (Casas et al., 2006). Recently, several studies have demonstrated the importance of higher resolution DEMs for a more accurate hydro-geomorphological and flooding hazard analysis (e.g., Manfreda et al., 2011; Biron et al., 2013; Saksena and Merwade, 2015; Papaioannou et al., 2016; Ogania et al., 2019; Farooq et al., 2019; Annis et al., 2020; Avand et al., 2022).

Another key factor of hazard is the riverbed structure and especially the particle size that constitute its armor layer (often expressed in the form of roughness coefficient, k_s), which influences flow regime (Aberle and Smart, 2003; Kim et al., 2010; Lau and Afshar, 2013). It becomes, thus, essential to carry out an accurate riverbed particle-size analysis to determine reliable hydro-geomorphological and flooding-hazard parameters.

Particle-size characterization can be complex and costly if carried out by traditional in-situ sampling, given both the difficulty in physically reaching the riverbed (frequently inaccessible areas) and the necessity to analyze limited areas concerning the whole region of interest. Using photo-sieving techniques, UAV imagery can compensate for these shortcomings (e.g., Woodget and Austrums, 2017; Woodget et al., 2018; Carrivick and Smith, 2019). Today, there are different tools to perform photo-sieving analysis, which automatically digitize particle size using segmentation-based image processing (e.g., Butler et al., 2001; Graham et al., 2005; Detert and Weitbrecht, 2012).

The main goal of this paper is to use an original approach for the assessment of hydro-geomorphological hazard by means of UAV-based high-resolution topographic data. The case under study refers to an extended reach of Basento river (Southern Italy). We first performed sensitivity analyses both of the resolution of UAV-derived DEMs, of the roughness coefficient resulting from photo-sieving analysis and the morphological change detection analyses over short-time ranges (2019–2021). Data were finally used, together with a statistical analysis of the local rainfall trend, to produce a probabilistic assessment of flood hazard.

2. Data and methods

2.1. Case study

Basento river (Basilicata, southeastern Italy) rises at Monte Arioso (1709 m ASL), in the southern Apennine Mountains, and occupies a catchment of about 1546 km^2 with a NW-SE trending valley of 150 km length (Medici et al., 2011). It flows into the Ionian Sea crossing the coastal plain at about 30 km SW of Taranto, near Metaponto (De Musso et al., 2018).

The river course can be divided into three main sections: upper, middle and lower Basento (Fig. 1). The upper Basento crosses the mountain areas and the Apennines up to Campomaggiore, the middle Basento crosses the hilly areas from Tricarico to Bernalda, and finally, the lower Basento crosses the coastal plain near Metaponto.

The geomorphology is predominantly hilly, and the flatter zones are located near the river and the Ionian coast. This area is crossed by the incision of the river that forms a valley with steep slopes and a relatively flat fluvial plain, with an average width of 1.5 km. Up to the coastal plain, the valley is characterized by the presence of fluvial terraces, which delimit the current flood plain (Piccarreta et al., 2012).

The hydrological regime of the catchment follows the seasonal rainfall trend (mean annual rainfall of about 766 mm with extreme events recorded between October and March, Piccarreta et al., 2013), showing a significant relationship between rainfall and river flow: maximum values between November and January, and minimum in July or August, with an average annual flow rate of 12.2 m^3/s (recorded at Menzena station, 24 km from the river mouth) (AdB-Basilicata).

The area under investigation consists of an extended river reach that is subject to high hydro-geomorphological risk. It is located along the hilly plain of Basento river near the industrial area of Ferrandina (MT), located in the middle section. This area has been subject to significant morphological modifications in the past, which led to several failures, including the collapse of a road along the river banks (Fig. 2).

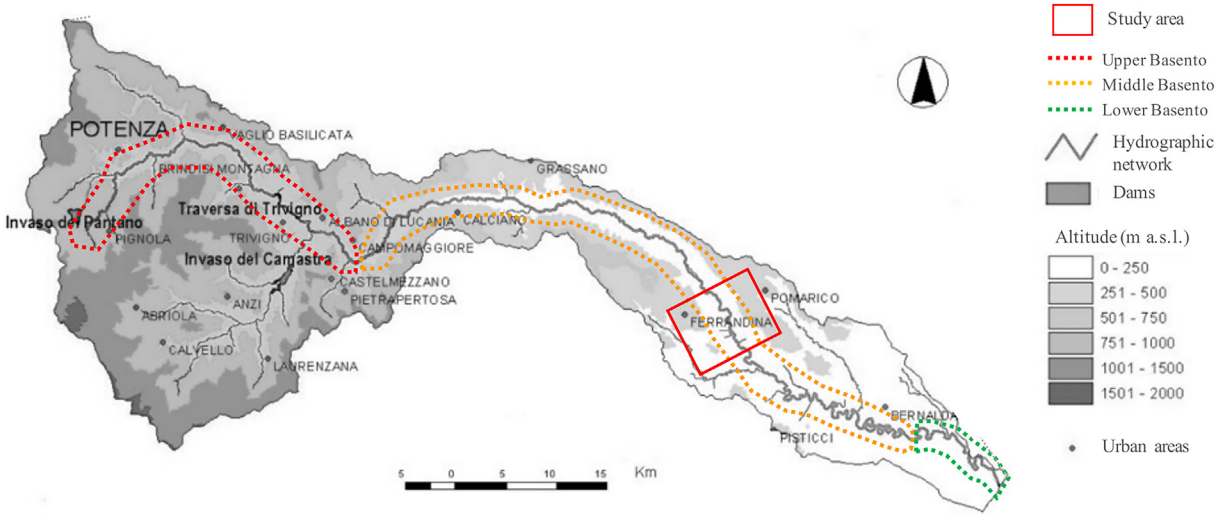

Fig. 1. Watershed of the Basento river. The dashed line in red highlights the upper section of the river, in yellow the middle section and in green the lower section. Source images: "Autorità di Bacino distrettuale dell'Appennino Meridionale sede Basilicata" modified.

Fig. 2. Effects of fluvial and alluvial dynamics related to some reaches of the Basento river, Basilicata, southeastern Italy. a) Failure of part of a roadway; b) Bridge collapse along the river; c) Levee failure due to bank erosion.

2.2. Data acquisition and processing

To investigate an extended reach of Basento river, multiple sequences of aerial images were collected with UAV. For this, we used a quadcopter "DJI Inspire 2" with aluminum-magnesium composite body and carbon fiber arms was used. It has a maximum take-off weight of about 4250 g and the onboard sensor is an optical camera "Zenmuse X5S" with 20.8 MP (supported lens DJI MFT 15 mm/1.7 ASPH, sensor CMOS 4/3″, FOV 72° and image resolution 5280 × 3956 pixel). To acquire the desired Ground Sampling Distance (GSD) of about 1.09 cm/pix, the flight altitude was set to 50 m above ground level of take-off location (Fig. 3-a).

Three surveys with multiple automatic photogrammetric flight missions were performed during the lean season (June–July) and covered the same reach in three different time intervals in 2019, 2020 and 2021 (Fig. 3-b). In 2019, 12 flight missions were carried out, resulting in a dataset of about 3000 images and covering an area of approximately 2000 per 320 m. In 2020, 20 flight missions were carried out, obtaining a dataset of 4000 images and covering a larger area of approximately 3000 per 320 m. While in 2021, 14 flight missions were performed, resulting in a dataset of about 3000 images and covering an area of approximately 2300 per 320 m.

To georeference the output generated by processing of the above datasets through an absolute orientation, positional data were extrapolated

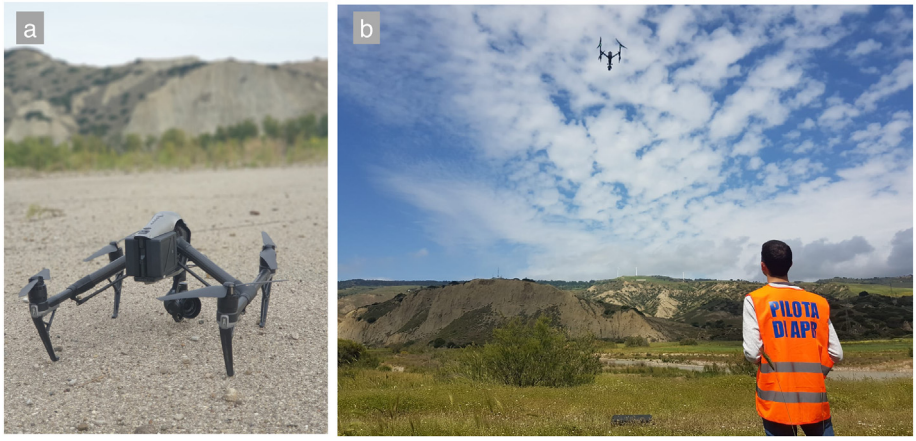

Fig. 3. a) UAV used for the surveys; b) Performing a photogrammetric flight mission of the area of interest.

from the technical regional cartography (GCPs – Ground Control Points). This was necessary due to the inaccessibility of several areas of the river reach and the inability to detect direct georeferencing points uniformly distributed over the whole scene of interest. To significantly improve the accuracy of model reconstruction, manual tie points (MTPs, 3D point corresponding to feature that is marked by the user in many images, instructing the software that it is the same) were used in addition to GCPs. Specifically, for the dataset related to 2019, 20 GCPs and 9 MTPs were used; for the dataset related to 2020, 20 GCPs and 20 MTPs; while for the dataset related to 2021, 20 GCPs and 13 MTPs.

The acquired datasets were then processed using the Pix4D photogrammetric software (which follows the main steps of the SfM process, as described in Eltner and Sofia, 2020) to generate orthomosaics and DEMs, with a resolution of 1.23 cm/pix and 6 cm/pix respectively. The accuracy of the models for the three datasets is reported in Table 1.

To assess the advantage, for the aim of hydro-geomorphological analysis, of the very high-resolution (6 cm) of the DEMs derived from UAV survey, we compared data with those that can be obtained by DEMs extracted using more "traditional" techniques: LIDAR and technical cartography data. For this aim an operation of down-sampling at a resolution of 1 m (to allow the same DEM resolution derived from LIDAR) and at 5 m (as the DEM resolution derived by technical cartography data, Ground Control Points and Model Keypoints) was performed. The effect of the different resolutions on the river flow-regime parameters will be discussed in the following sections.

2.3. Probabilistic model of river flooding hazard

2.3.1. River flow-regime parameters

In our model, river flooding hazard is related both to geomorphological features and a probability function of flow-regime parameters, all extracted from DEMs.

This section describes the following river flow-regime parameters: shear velocity, height-averaged velocity, filled capacity discharge, time of concentration and peak discharge, which were used for defining a flood probability model and assessing the hydro-geomorphological hazard of several cross-section of the river reach.

Shear velocity (U^*) refers to a form of shear stress, rewritten in unit of velocity, evaluated at the lower boundary of a river channel (von Kármán, 1930). It is calculated as the square root of the ratio between the shear stress at the boundary (τ) and fluid density (ρ) (Eq. (1)). In this case the ratio is equal to the square root of the product between the gravitational acceleration (g), the sine of the river slope angle ($sin(\alpha)$) and the hydraulic radius (Hr), representing the ratio between the flood discharge area and the wetted perimeter of the cross-section.

$$U^* = \sqrt{\frac{\tau}{\rho}} = \sqrt{gsin\alpha Hr} \tag{1}$$

Height-averaged velocity ($\overline{\overline{U_{(y)}(t)}}$) is defined as the flow velocity averaged along with the time-averaged velocity profile, which refers to a turbulent flow and is proportional to the logarithm of the distance from a specific point to the boundaries of the fluid region (von Kármán, 1930). It represents a factor that describes the magnitude of velocity and the characteristics of the flow, following the log-law as reported in Schlichting and Gersten (2016) (Eq. (2)), where k is the von Kármán constant (0.4) and k_s the roughness coefficient, which in this case, refers to the particle size of the riverbed.

$$\overline{\overline{U_{(y)}(t)}} = U^* \left(\frac{1}{k} \ln \left(\frac{Hr}{k_s} \right) + 6 \right) \tag{2}$$

Filled capacity discharge (π) represents the maximum rate of flow that occurs when the maximum flood stage is reached in a stream as a result of storm events. The filled-capacity discharge of a given river cross-section can be estimated as the product between the height-averaged velocity and the river cross-section area (A) (Eq. (3)).

$$\pi = \overline{\overline{U_{(y)}(t)}}\, A \tag{3}$$

Time of concentration (t_c), represents the time it takes for a generic water droplet falling at the hydraulically farthest point to reach the closing section of the watershed. In this case, it refers to the ratio between the river's length from the source to the closing section (L) and the height-averaged velocity (Eq. (4)).

$$t_c = \frac{L}{\overline{\overline{U_{(y)}(t)}}} \tag{4}$$

Peak discharge *(Q)*, following the rational method (ASCE, 1992), represents the discharge calculated considering the upstream catchment area of the investigated river reach (A_c), the cumulative rainfall in the time of concentration (i), and the runoff coefficient (C, related to the different land-use of the upstream catchment area) (Eq. (5)). When the peak discharge is equal to the filled capacity (π), i represents the cumulative rainfall value (Eq. (6)) that, if exceeded, involves flooding in a given river cross-section.

$$Q = \frac{i\, A_c\, C}{t_c} \tag{5}$$

$$i = \frac{\pi\, t_c}{A_c\, C} \tag{6}$$

2.3.2. Rainfall trend analysis

Rainfall is one of the most important climatic factors influencing spatio-temporal water availability, and its trend over years is key for detecting climatic extreme events (e.g., flood). Indeed, this factor directly influences the hydro-geomorphological hazard analyses and, specifically, the peak discharge and the time of concentration of a river channel.

To determine the probability of flooding of several cross sections of the Basento river reach, the identification of the maximum rainfall recorded in

Table 1
Accuracy of the models for the three datasets (2019, 2020, 2021). The Root Mean Square Error values for each direction are shown.

Dataset	Direction	RMSE [m]
2019	X	0.026
	Y	0.024
	Z	0.134
2020	X	0.021
	Y	0.018
	Z	0.046
2021	X	0.010
	Y	0.019
	Z	0.045

Fig. 4. Polygons related to the Ferrandina SP and Potenza rainfall gauging stations (red dots) derived by the Thiessen method.

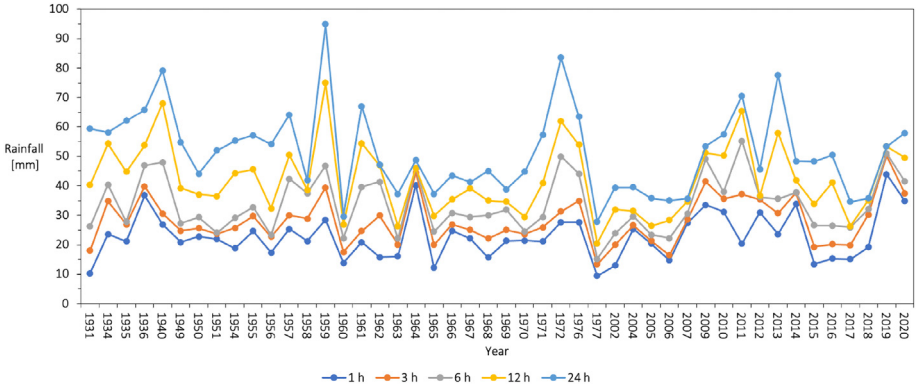

Fig. 5. Maximum rainfall of the considered catchment area derived by summing the values obtained for the two gauging stations, considering the area significance values.

the 1st, 3rd, 6th, 12th and 24th hour in 45 years (from 1931 to 2020) ("Dipartimento di Protezione Civile Regione Basilicata, Pluviometria") was performed at the gauging stations of Ferrandina SP (MT) and Potenza (PZ). These stations cover the area of the upstream watershed of the river reach that contributes to the surface runoff production. For each gauge station, the relative area significance, compared to the total area of the watershed upstream, was assigned through the Thiessen polygon approach. Perpendicular bisectors were constructed at the midpoint of the lines joining each gauge station. These bisectors, which intersect the boundaries of the Basento catchment area, form polygons containing a station (Fig. 4). The rainfall value measured at a gauging station is then assigned to the whole area covered by the polygon enclosing it.

After obtaining the area significance values for each station (30 % Ferrandina SP, 70 % Potenza) (Eqs. (7) and (8)) and multiplying them by the relative rainfall values, the total rainfall of the catchment area was derived by summing the values of the two gauging stations (Fig. 5).

By converting the resulting rainfall values to the logarithm, which allowed obtaining Gaussian distributions (after a normality test at a probability level of 0.05) and plotting them for all time slots, a cumulative rainfall graph was derived (Fig. 6).

$$\text{Ferrandina SP} = \frac{\text{catchment area Ferrandina SP}}{(\text{catch.area Ferrandina SP} + \text{catch.area Potenza})} = 0.3 \tag{7}$$

$$\text{Potenza} = \frac{\text{catchment area Potenza}}{(\text{catch.area Ferrandina SP} + \text{catch.area Potenza})} = 0.7 \tag{8}$$

In the graph, by fitting with a power law the points corresponding to a specific year for different time slots, the function of the Eq. (9) is derived, where i_c represents the cumulative rainfall related to a specific time slot.

$$i_c = a(t_c)^b \tag{9}$$

For each river cross section, through the time of concentration (t_c), it was possible to extract from the graph the corresponding rainfall value (i_c) for each year of the time series and obtain the rainfall Gaussian distribution, by which i (Eq. (6)) was calculated both for each DEM resolution and k_s value (see next section), as representing the cumulative rainfall value that, if exceeded, involved flooding in a given river cross-section. Finally, the value 1-i, as recalculated as a percentage (exceedance probability), was obtained as expressing the flooding probability.

2.3.3. Riverbed particle-size analysis

The riverbed particle size, which defines k_s of Eq. (2), is important in defining the river flow parameters and, consequently, the level of hydro-geomorphological hazard.

In this paper, two approaches were used and compared to determine the mean particle diameter and the 84th percentile value (following the

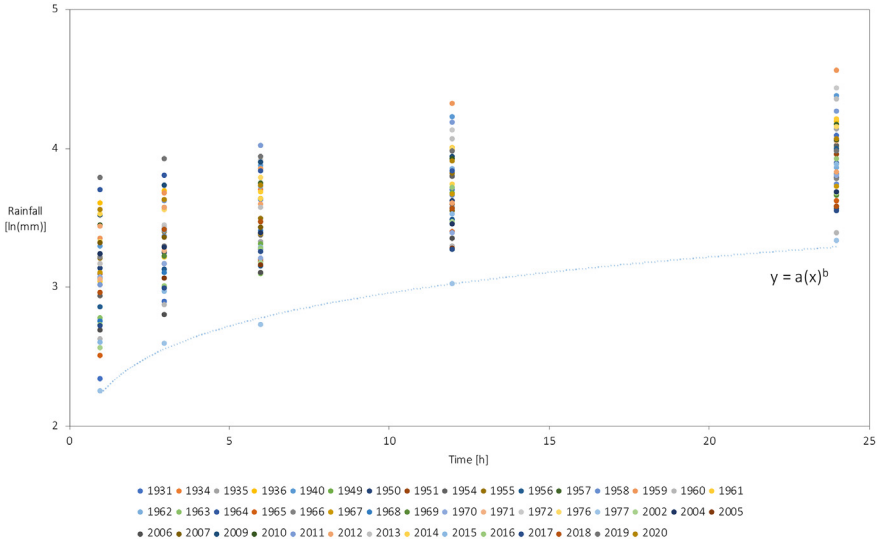

Fig. 6. Cumulative rainfall graph derived by plotting the logarithm rainfall values for all time slots of the time series considered. The light blue dashed line shows an example of how the power law equation fits well the points (in this specific case related to year 1977).

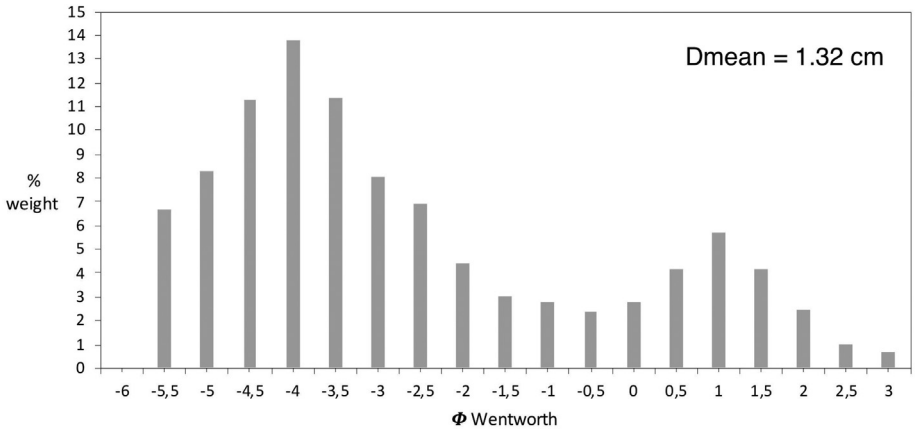

Fig. 7. Particle-size distribution of the whole sample.

statements in Leopold et al., 1964, about the use of a size larger than D_{50} when a single flow resistance parameter involves bed particle size): in situ sampling with laboratory particle-size analysis and photo-sieving analysis by using UAV imagery.

In situ, the sampling was carried out along an accessible area of the fluvial plain during the lean season (June 2019). About 10 kg of mostly gravelly material was collected. ASTM standard sieves with mesh from −6 ø to 3 ø were used, following the classification proposed by Wentworth (1922) (Fig. 7).

UAV images of a point bar were acquired, at different altitudes and resolution (25 m with 0.5 cm/pixel, 12.5 m with 0.27 cm/pixel and ~2 m with 0.5 mm/pixel) and used to perform photo-sieving analysis. These images were processed into "Fiji – ImageJ" image analysis tool (Schindelin et al., 2012) following a series of steps: setting image scale, transforming it into a binary image and defining the limits between the particles (through "watershed" approach that finds the center of each particle, then calculates a distance map from the particle center points to the edge of the particles and fills that "topological map" with imaginary water), particle counting and determining the Feret diameter (distance between two parallel lines tangent to the perimeter of the area projected by the particle). The most consistent results between in-situ sampling and photo sieving were obtained by analyzing images at altitude ~2 m (0.5 mm resolution) and 12.5 m (0.27 cm resolution) (Fig. 8).

Due to image resolution, it is not feasible to detect the diameter of sand particles with photo sieving. Therefore, to strictly consider the particles size of the river armor layer and make the results from the two approaches comparable (in situ and photo sieving), the mean diameter and the 84th percentile values were calculated by considering the distribution between the classes −6 ø (6.4 cm) and − 3.5 ø (1.13 cm) for the laboratory particle-size analysis and the values greater than or equal to 1.13 cm for photo sieving (Table 2).

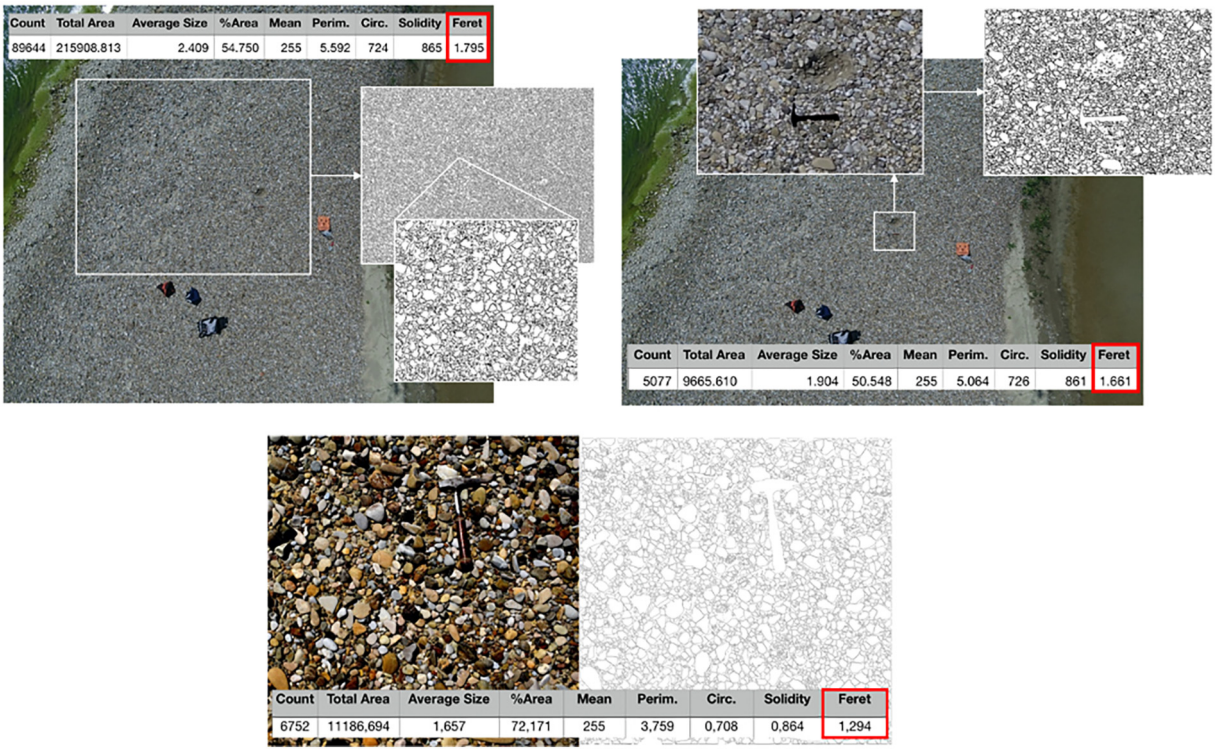

Fig. 8. 1) UAV image taken at 12.5 m altitude (0.27 cm/pixel). The box in red highlights the mean diameter (Feret) considering an area greater than the in-situ sampling one; 2) UAV image taken at 12.5 m altitude (0.27 cm/pixel). The box in red highlights the resulting mean diameter considering strictly the in-situ sampling area; 3) UAV image taken at ~2 m altitude (0.5 mm/pixel). The box in red highlights the mean diameter.

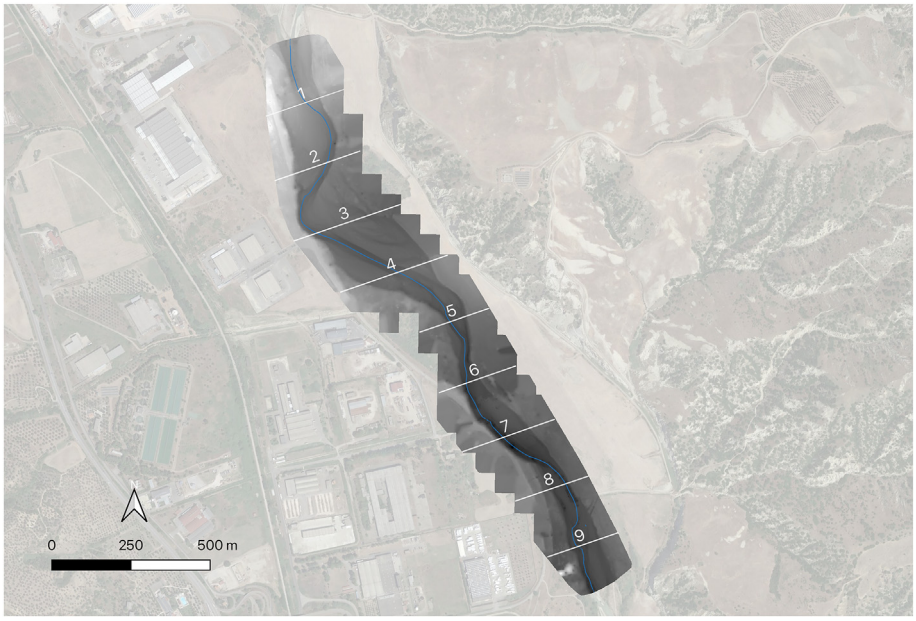

Fig. 9. Location of cross-sections trace (white segments) on DEM. The segment in light blue indicates the channel centerline.

3. Results

3.1. Hydro-geomorphological hazard of Basento river

To assess the flooding hazard of the river reach, several cross-sections were identified (every 200 m, following the changes in direction of the channel centerline), where flow-regime parameters were computed (Fig. 9).

This section reports the estimation of flooding hazard and the analyses of geomorphological changes that occurred between the three years of study (2019–2021). A sensitivity analysis of both the flow- regime parameters and the flood hazard to DEM resolutions and to roughness coefficient is first carried on, which is followed by a spatiotemporal analysis of morphological changes of the river reach.

3.1.1. Sensitivity analysis

Sensitivity analysis was performed in order to assess the influence of DEM resolution and of roughness coefficient values (k_s) on flow-regime parameters and flooding hazard of the 9 cross-sections of the river reach.

Flow-regime parameters were calculated (Table 3) for all cross sections from the DEMs extracted at various resolution from UAV data (Fig. 10).

The flooding hazard was assessed for each cross section (Table 4) by exploiting the cumulative rainfall graph (see Fig. 6) and by following the approach in Section 2.3.2.

Except for profiles 3 and 5, which showed a reduction of the flooding hazard passing from 6 cm to 1 m of DEM resolution, the higher was the DEM resolution, the lower the percentage probability of flooding (Table 4). These variations are mostly due to the smoother trend of the topographic profiles extracted from DEMs with coarser resolution, affecting the identification of the cross-section areas and, consequently, their filled capacity discharge (π) (which directly influences the cumulative rainfall values needed for flooding). This involves higher time of concentration related to a lower rainfall value (i) and a higher flooding hazard probability. Specifically, the most important changes between the end member's

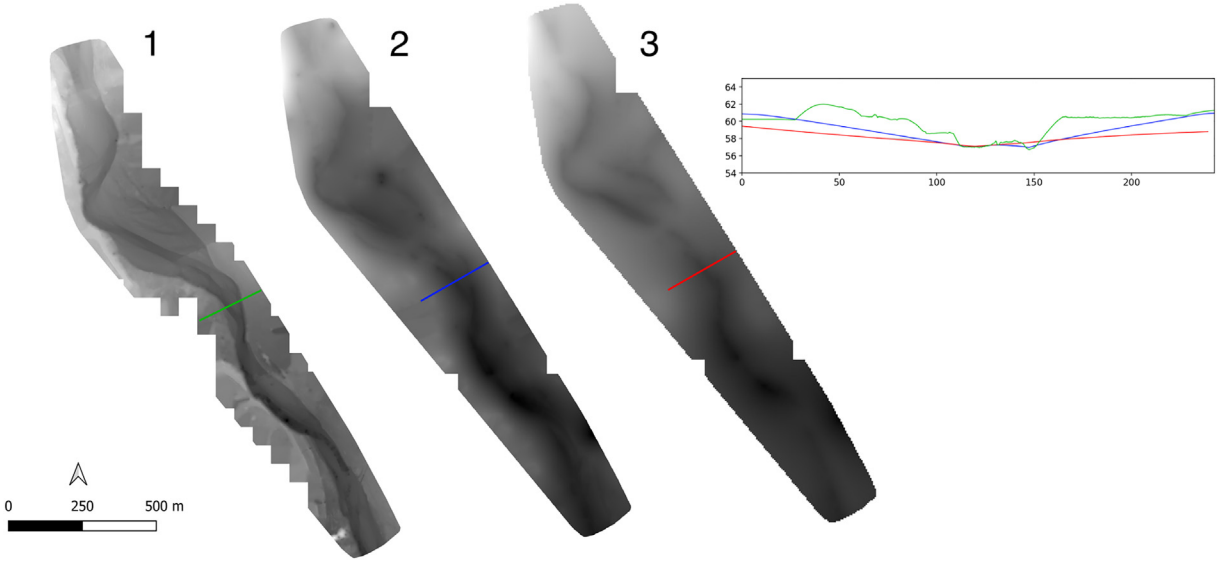

Fig. 10. DEMs with different resolutions derived by UAV surveys of the river reach of interest in 2019: 1) Original DEM with 6 cm resolution; 2) Subsampled DEM at 1 m resolution; 3) Subsampled DEM at 5 m resolution. The box on the right shows a cross-section comparison of the different DEMs.

resolutions of 6 cm and 5 m were recorded for profiles 4, 7, 8 and 9 with a percentage difference of about 99.9 %, 99.6 %, 94.5 % and 91.4 %, for the two resolutions, respectively (see Table 4).

To assess the influence on flooding of the roughness coefficient (k_s) derived from laboratory particle size and from photo-sieving analyses, flow-regime parameters were calculated considering both the mean diameter and the diameter of the 84th percentile of the river armor layer particle size (see Table 2).

Tables 5 and 6 report the results obtained for flow-regime parameters and flooding hazard values using the 6 cm resolution DEM. Larger particle size was associated with a higher probability of flooding (see Table 6). These variations are due to the increased friction component at the lower boundary of the river channel, which in turn affects the height-averaged velocity of the flow, the filled capacity discharge and, consequently, the cumulative rainfall value needed for flooding. The most important changes, considering the end member's sizes (2.28 cm and 3.61 cm mean particle diameter), were recorded for profiles 1, 2, 3, 5 and 6 with a percentage difference of about 2.3 %, 2.7 %, 3.2 %, 2.3 % and 2.6 %, respectively (see Table 6).

The same analysis was carried out considering the diameter of the 84th percentile. Tables 7 and 8 report the resulting flow-regime parameters and the flooding hazard values.

Also, in this case, a larger particle size resulted in a higher flooding hazard, with higher differences than the previous analysis (see Table 8), which were due to the greater differences in the k_s values. The most important changes, considering the end-members sizes (1.29 cm and 5.17 cm particle diameter), were recorded for profiles 1, 2, 3, 5 and 6, with percentage differences of 6.8 %, 7.8 %, 9.4 %, 7.3 % and 6.6 %, respectively.

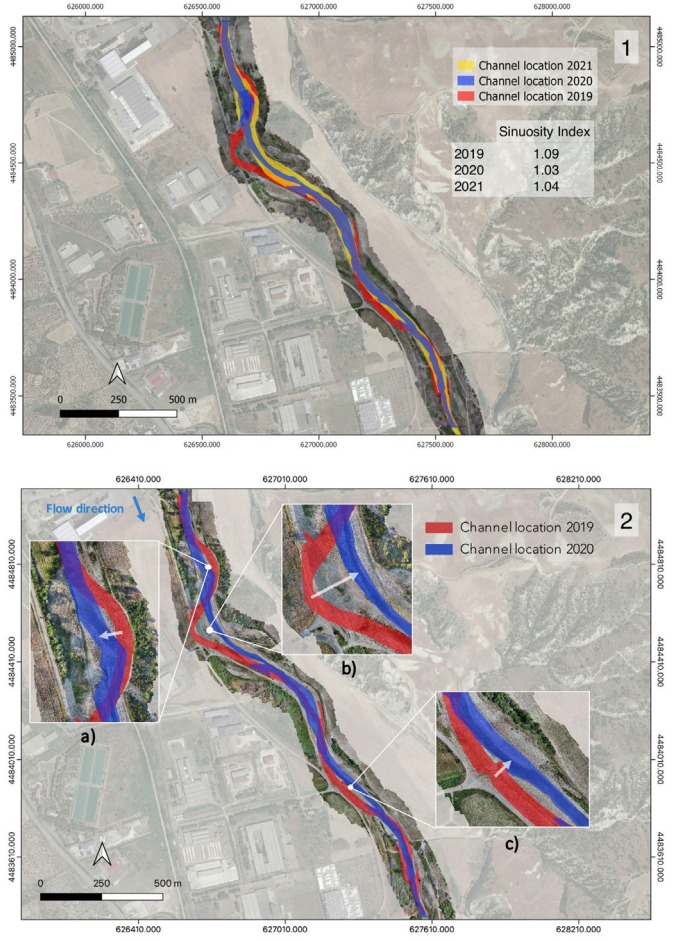

Fig. 11. 1) Channel displacements maps based on UAV orthomosaics of 2019, 2020 and 2021 projected on the orthomosaic of 2021 (1.3 cm/pixel). In the right corner the table reports the relative sinuosity index values. 2) Channel displacements maps based on UAV orthomosaics of 2019 and 2020 projected on the orthomosaic of 2020 (1.3 cm/pixel). Boxes a, b and c highlight the largest changes of the main river channel.

3.1.2. Change detection analysis

The availability of on-demand high-resolution data of the river channel, possible through UAVs, allows to perform morphological change detection analysis over short-times and to assess the effect on the hazard. For this aim, multitemporal orthomosaics were composed of identifying the different location of river morphological planimetric elements and the process that determined them (erosion and deposition).

In the planimetric analysis, the morphology of the main river channel was represented as its sinuosity index (i.e., the ratio of the length measured along the watercourse to the length measured for the same reach following its planimetric direction, Rinaldi et al., 2016) and compared between years 2019, 2020 and 2021 (Fig. 11-1). The largest changes were recorded between years 2019 and 2020, where it is shown (Fig. 11-2) that in sector (a) there was a shift of the main channel by about 47 m, a shift by about 94 m in sector (b), and a shift of about 45 m in sector (c). These displacements were mainly caused by anthropogenic modifications made for river bank safety, which significantly altered the channel, embedding it into forced paths.

Between years 2020 and 2021, the shifts were minimal, as also highlighted by the very similar values of the sinuosity index (Fig. 11-1).

Erosional and depositional processes can be detected by analyzing the displacements, which can be quantified through a DEM of Difference analysis (DoD, subtraction of the elevations of an older DEM from the elevations

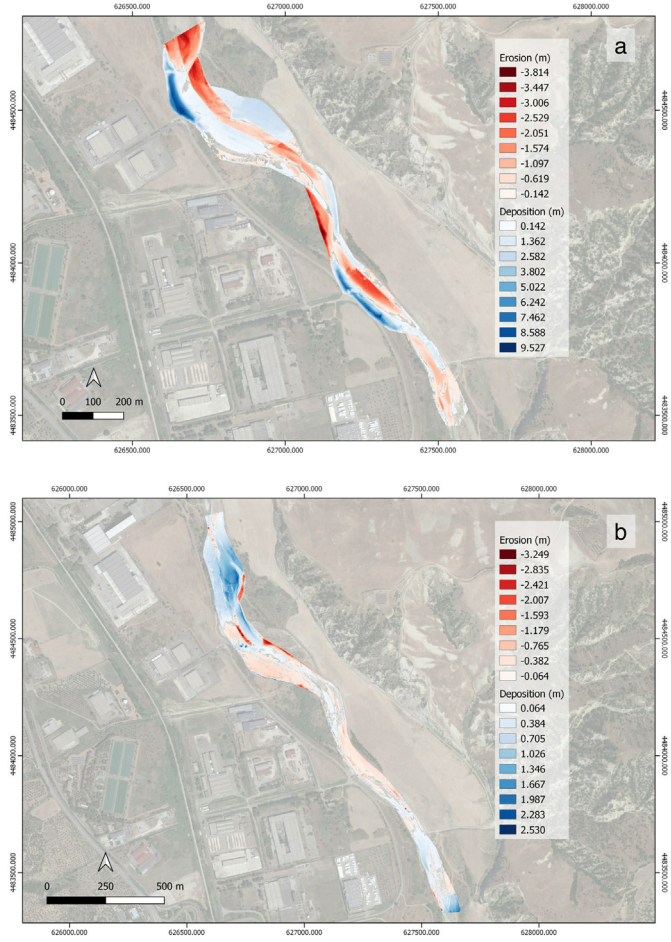

Fig. 12. a) DEM of Difference between 2019 and 2020 using 6 cm resolution DEMs; b) DEM of Difference between 2020 and 2021 using 6 cm resolution DEMs.

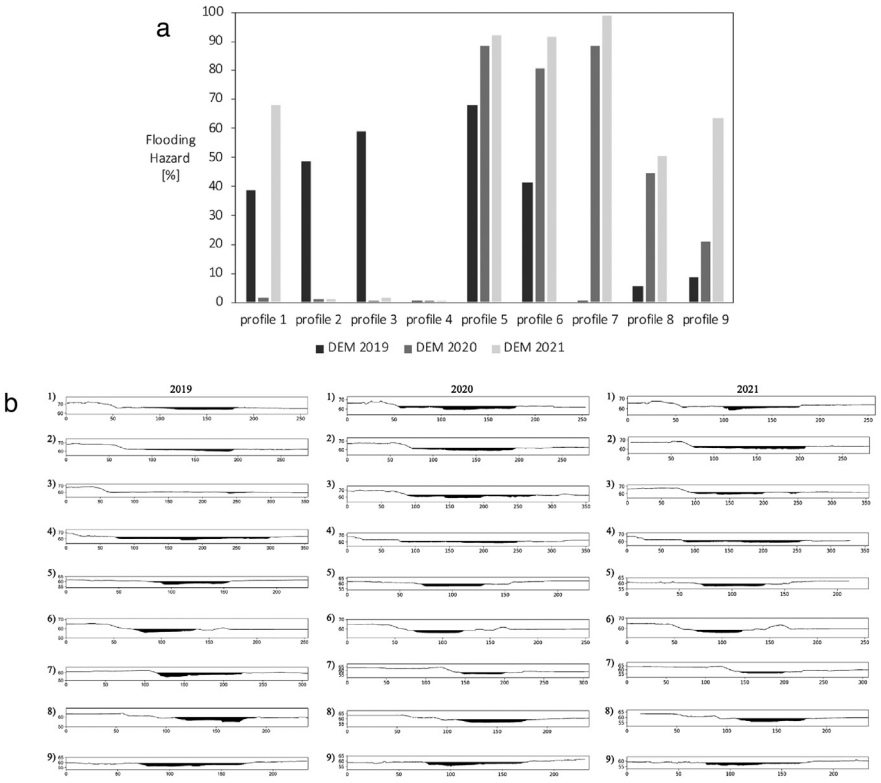

Fig. 13. a) Comparison of the flooding hazard values computed for each cross-section considering the multitemporal DEMs with 6 cm resolution and k_s of 2.28 cm, b) comparison of filled capacity discharge of all cross-sections derived from the multitemporal DEMs (2019–2021) with 6 cm resolution.

of a newer DEM on a cell-by-cell basis in order to quantify the volumetric changes). This analysis was performed using the 6 cm resolution DEMs and by applying a Minimum Level of Detection (LOD_{min}) of changes, as estimated from the root sum square of the $RMSE_z$ values ($\delta Z1$, $\delta Z2$) of the older and newer DEM respectively (Eq. (11)) (Williams, 2012). LOD_{min} was thus applied as a constant threshold across the DoD.

Fig. 12-a shows the results of DoD obtained by using the active river fluvial plain between 2019 and 2020, in which about 74,385.11 m^3 of solids were eroded and 134,181.35 m^3 deposited; while Fig. 12-b shows the results relative to years 2020–2021, in which about 22,810.79 m^3 of solids were eroded and about 50,181.16 m^3 deposited. The major volumes recorded for the 2019–2020 analysis are mainly related to the anthropogenic modifications made for river bank safety.

$$LOD_{min} = \sqrt{(\delta Z1)^2 + (\delta Z2)^2} \quad (11)$$

To demonstrate the influence of the river-channel displacements on flooding hazard for each cross-section, a comparison of the flooding hazard values obtained by means of the multitemporal DEMs (2019–2021), with 6 cm resolution and k_s value of 2.28 cm, was performed.

Table 2
Mean diameter and D_{84} values related to the river armor layer particle size derived from lab particle size and photo-sieving analyses. *analysis area greater than sampling area; ** sampling area.

Technique		Mean diameter [cm]	D_{84} [cm]
In-situ sampling		2.28	1.29
Photo-sieving	0.27 cm/pixel*	3.61	5.17
	0.27 cm/pixel**	3.28	4.45
	0.5 mm/pixel	2.44	1.98

The most important changes occurred between years 2019 and 2020 that, as previously stated, were due to an anthropogenic impact. A reduction in the percentage of flooding hazard was recorded in 2020 (a large increase of the filled capacity discharge) for profiles 1, 2, and 3, which is about 37.4 %, 47.4 % and 58.9 %, respectively (Fig. 13-a). For the other cross sections, an increase of flooding hazard due to the reduction of the filled capacity discharge was recorded, with a maximum difference, for profiles 5, 6, 7, 8 and 9, of about 20 %, 39 %, 88.3 %, 38.8 % and 12.5 %, respectively. In particular, profile 7 passed from a null flood hazard probability in 2019 to a high flood probability in 2020. On the other hand, between years 2020 and 2021 the flooding probability changes were minimal (in line with the morphological changes mentioned above), except for profiles 1 and 9, where increases of about 66.8 % and 42.2 % were calculated, respectively (Fig. 13-a and b).

4. Discussion and conclusions

Some approximations were introduced in this study that may have in part constrained the results, such as: the presence of water bodies in the riverbed, which may have caused some error in the reconstruction of the topographic profile and the cross-section area; the availability of the rainfall values of just two gauging stations in the upstream catchment of the river reach; and the use of a rainfall intensity equal to the time of concentration, without taking into consideration the influence of soil moisture. We believe that such approximations did not dramatically influence the results, especially in terms of the sensitivity analysis, which demonstrated the importance of high-resolution DEMs derived by UAV surveys.

Our analysis showed that extrapolating the topographic profiles of the river cross sections from lower resolution DEMs involves a significant increase in flooding probability. This is due to the smoother trend of the topographic profiles derived by DEMs with coarser resolution, which in turn affects the identification of the cross-section areas and consequently their filled capacity discharge (π), which directly influences the cumulative rainfall values needed for flooding.

Table 3
Flow regime parameters calculated from DEMs with 6 cm, 1 m and 5 m resolution. A = cross-section area; Hr = Hydraulic radius; S = channel slope angle; k_s = roughness coefficient; g = gravitational acceleration; k = Von Kármán constant; U* = shear velocity; U = Height-averaged velocity; π = filled capacity discharge; L = river channel length from source to cross-section; t_c = time of concentration.

Profile	A [m^2]	Hr [m]	S [°]	k_s [m]	g [m/s^2]	k	U* [m/s]	U [m/s]	π [m^3/s]	L [m]	t_c [h]
DEM 6 cm											
1	190.061	2.1	0.263	0.0228	9.81	0.4	0.308	5.322	1011.540	69,553.631	3.63
2	182.744	1.73					0.279	4.695	858.054	69,753.631	4.13
3	190.137	0.91					0.202	3.080	585.677	69,953.631	6.31
4	706.301	3.05					0.371	6.760	4774.446	70,153.631	2.88
5	153.314	2.03					0.302	5.207	798.322	70,353.631	3.75
6	177.644	2.63					0.344	6.150	1092.451	70,553.631	3.19
7	409.918	3.62					0.404	7.537	3089.691	70,753.631	2.61
8	259.175	3.01					0.368	6.703	1737.293	70,953.631	2.94
9	249.216	2.35					0.325	5.722	1425.902	71,153.631	3.45
DEM 1 m											
1	190.7	1.14	0.264	0.0228	9.81	0.4	0.227	3.582	683.103	69,553.631	5.39
2	78.644	0.87					0.198	2.995	235.560	69,753.631	6.47
3	205.126	2.01					0.301	5.184	1063.326	69,953.631	3.75
4	460.863	1.79					0.284	4.809	2216.489	70,153.631	4.05
5	172.01	1.41					0.252	4.118	708.322	70,353.631	4.75
6	110.619	1.13					0.226	3.561	393.954	70,553.631	5.50
7	179.81	1.43					0.254	4.156	747.284	70,753.631	4.73
8	52.171	0.76					0.185	2.737	142.786	70,953.631	7.20
9	73.418	1.11					0.224	3.520	258.409	71,153.631	5.62
DEM 5 m											
1	80.906	0.86	0.269	0.0228	9.81	0.4	0.199	3.000	242.744	69,553.631	6.44
2	57.983	0.67					0.176	2.539	147.195	69,753.631	7.63
3	162.912	0.72					0.182	2.664	434.059	69,953.631	7.29
4	89.205	0.83					0.196	2.930	261.386	70,153.631	6.65
5	48.089	0.67					0.176	2.539	122.078	70,353.631	7.70
6	96.008	0.97					0.211	3.250	312.029	70,553.631	6.03
7	95.64	0.9					0.204	3.092	295.761	70,753.631	6.36
8	35.191	0.53					0.156	2.166	76.234	70,953.631	9.10
9	34.207	0.42					0.139	1.848	63.199	71,153.631	10.70

Table 4
Flooding hazard percentage values calculated for all cross-sections extrapolated from DEMs with 6 cm, 1 m and 5 m resolution. i = rainfall values resulting in filled capacity discharge; ln = natural logarithm; Gaussian distribution = Normal distribution of the i value with respect to i_c values calculated for the time series considered; Flooding hazard = 1 – gaussian distribution (exceedance probability).

Profile	i [mm/t_c]	ln	Gaussian distribution	Flooding hazard [%]
DEM 6 cm				
1	31.25	3.442	0.613	38.7
2	30.16	3.407	0.516	48.3
3	31.45	3.448	0.411	58.9
4	117.02	4.762	1.000	2.3E-05
5	25.48	3.238	0.318	68.2
6	29.66	3.390	0.585	41.5
7	68.63	4.229	0.999	0.06
8	43.47	3.772	0.946	5.4
9	41.87	3.734	0.914	8.5
DEM 1 m				
1	31.34	3.445	0.469	53.1
2	12.97	2.563	1.55E-04	99.9
3	33.94	3.524	0.710	29.0
4	76.40	4.336	1.000	0.03
5	28.63	3.355	0.388	61.2
6	18.44	2.915	0.019	98.1
7	30.08	3.404	0.460	53.9
8	8.75	2.169	1.24E-05	99.9
9	12.36	2.514	1.56 E-04	99.9
DEM 5 m				
1	13.30	2.588	2.28E-04	99.9
2	9.56	2.257	3.18E-07	99.9
3	26.93	3.293	0.165	83.4
4	14.79	2.694	8.36E-04	99.9
5	8.00	2.079	7.06E-09	99.9
6	16.01	2.773	3.24E-03	99.6
7	16.01	2.773	2.64E-03	99.7
8	5.90	1.776	9.65E-13	100
9	5.76	1.750	1.41E-13	100

Table 5
Flow regime parameters influenced by the different values of k_s (mean diameter), calculated for all cross-sections extrapolated from the 6 cm resolution DEM. U = Height-averaged velocity; π = filled capacity discharge; t_c = time of concentration.

Profile	k_s = 2.28 cm			k_s = 2.44 cm			k_s = 3.28 cm			k_s = 3.61 cm		
	U [m/s]	π [m^3/s]	t_c [h]	U [m/s]	π [m^3/s]	t_c [h]	U [m/s]	π [m^3/s]	t_c [h]	U [m/s]	π [m^3/s]	t_c [h]
1	5.322	1011.540	3.63	5.270	1001.630	3.67	5.043	958.403	3.83	4.969	944.396	3.89
2	4.695	858.054	4.13	4.648	849.405	4.17	4.442	811.681	4.36	4.375	799.457	4.43
3	3.080	585.677	6.31	3.046	579.151	6.38	2.896	550.684	6.71	2.848	541.460	6.82
4	6.760	4774.446	2.88	6.697	4730.064	2.91	6.423	4536.469	3.03	6.334	4473.737	3.08
5	5.207	798.322	3.75	5.156	790.463	3.79	4.932	756.179	3.96	4.860	745.070	4.02
6	6.150	1092.451	3.19	6.091	1082.085	3.22	5.837	1036.870	3.36	5.754	1022.219	3.41
7	7.537	3089.691	2.61	7.469	3061.629	2.63	7.170	2939.222	2.74	7.074	2899.558	2.78
8	6.703	1737.293	2.94	6.641	1721.114	2.97	6.368	1650.543	3.09	6.280	1627.675	3.14
9	5.722	1425.902	3.45	5.666	1412.156	3.49	5.426	1352.195	3.64	5.348	1332.766	3.70

The analysis of the influence of k_s on flooding hazard showed a trend such that a larger particle size results in a higher probability of flooding, both considering the particle mean diameter and the 84th percentile. This is due to the increased friction component at the lower boundary of the river channel, which in turn affects the height-averaged velocity of the flow, the filled capacity discharge and consequently the cumulative rainfall value needed for flooding.

The difference in percentage values of flooding that resulted by comparing in-situ sampling and photo-sieving are lower than those obtained with different DEM resolutions, especially considering the value of particle mean diameter (maximum increase of the probability of flooding of about 3.2 %). Therefore, it can be inferred that the acquisition of UAV images at 12.5 m altitude, with a resolution of 0.27 cm/pixel for photo-sieving analysis, represents an optimal condition for ensuring the particle-size

Table 6
Flooding hazard percentage values calculated for all cross-sections extrapolated from DEMs with 6 cm, considering the different values of k_s (mean diameter). i = rainfall values resulting into filled capacity discharge; ln = natural logarithm; Gaussian distribution = Normal distribution of the i value with respect to i_c values calculated for the time series considered; Flooding hazard = 1 – gaussian distribution (exceedance probability).

Profile	i [mm/t_c]	ln	Gaussian distribution	Flooding hazard [%]
k_s = 2.28 cm				
1	31.25	3.442	0.613	38.7
2	30.16	3.407	0.516	48.3
3	31.45	3.448	0.411	58.9
4	117.02	4.762	1.000	2.3E-05
5	25.48	3.238	0.318	68.2
6	29.66	3.390	0.585	41.5
7	68.63	4.229	0.999	0.06
8	43.47	3.772	0.946	5.4
9	41.87	3.734	0.914	8.5
k_s = 2.44 cm				
1	31.28	3.443	0.611	38.9
2	30.14	3.406	0.512	48.8
3	31.45	3.448	0.406	59.4
4	117.14	4.763	1.000	2.3E-05
5	25.50	3.239	0.315	68.5
6	29.65	3.390	0.582	41.8
7	68.53	4.227	0.999	0.06
8	43.50	3.773	0.945	5.4
9	41.94	3.736	0.914	8.6
k_s = 3.28 cm				
1	31.24	3.442	0.593	40.6
2	30.12	3.405	0.493	50.6
3	31.45	3.448	0.386	61.4
4	116.98	4.762	0.999	2.5E-05
5	25.48	3.238	0.299	70.1
6	29.56	3.386	0.563	43.7
7	68.54	4.227	0.999	0.07
8	43.41	3.771	0.941	5.8
9	41.89	3.735	0.908	9.2
k_s = 3.61 cm				
1	31.27	3.443	0.589	41.0
2	30.14	3.406	0.489	51.1
3	31.43	3.448	0.378	62.2
4	116.89	4.761	0.999	2.5E-05
5	25.49	3.238	0.294	70.6
6	29.58	3.387	0.558	44.1
7	68.60	4.228	0.999	0.07
8	43.50	3.773	0.941	5.9
9	41.85	3.734	0.905	9.4

Table 7
Flow regime parameters in dependence of k_s (84th percentile), calculated for all cross-sections extrapolated from the 6 cm resolution DEM. U = Height-averaged velocity; π = filled capacity discharge; t_c = time of concentration.

Profile	k_s = 1.29 cm			k_s = 1.98 cm			k_s = 4.45 cm			k_s = 5.17 cm		
	U [m/s]	π [m^3/s]	t_c [h]	U [m/s]	π [m^3/s]	t_c [h]	U [m/s]	π [m^3/s]	t_c [h]	U [m/s]	π [m^3/s]	t_c [h]
1	5.760	1094.757	3.35	5.431	1032.154	3.56	4.808	913.829	4.02	4.693	891.917	4.12
2	5.093	930.677	3.80	4.794	876.043	4.04	4.229	772.782	4.58	4.124	753.659	4.70
3	3.369	640.479	5.77	3.152	599.252	6.17	2.742	521.330	7.09	2.666	506.900	7.29
4	7.287	5147.137	2.67	6.890	4866.765	2.83	6.140	4336.843	3.17	6.001	4238.707	3.25
5	5.638	864.322	3.47	5.314	814.671	3.68	4.702	720.828	4.16	4.588	703.449	4.26
6	6.640	1179.495	2.95	6.271	1114.013	3.13	5.574	990.247	3.52	5.445	967.327	3.60
7	8.112	3325.337	2.42	7.680	3148.062	2.56	6.862	2813.002	2.86	6.711	2750.952	2.93
8	7.227	1873.151	2.73	6.833	1770.946	2.88	6.088	1577.773	3.24	5.950	1541.999	3.31
9	6.185	1541.332	3.20	5.836	1454.495	3.39	5.178	1290.367	3.82	5.056	1259.972	3.91

characterization of wide areas, which is consistent with the grain size derived by in-situ sampling analysis.

The morphological changes recorded over short times (years 2019–2021) revealed significant variations of the topographic profile, with the major changes recorded between years 2019–2020, which were mainly related to anthropogenic modifications and induced significant changes of flooding hazard. An increase in the probability of flooding resulted in several cross sections, which in some cases (profile 7) passed form null to very high, illustrating how anthropogenic morphological modifications of river reaches can affect hazard if not projected adequately.

In conclusion, this study demonstrates the utility of an integrated UAV-SfM methodology combined with a statistic approach in the hazard assessment, which takes into account both geomorphological features and probability functions of flow-regime parameters. Our novel approach can be useful for the effective management of alluvial environments and,

Table 8
Flooding hazard percentage values calculated for all cross-sections extrapolated from DEMs with 6 cm, considering different values of k_s (84th percentile). i = rainfall values resulting into filled capacity discharge; ln = natural logarithm; Gaussian distribution = Normal distribution of the i value with respect to i_c values calculated for the time series considered; Flooding hazard = 1 – gaussian distribution (exceedance probability).

Profile	i [mm/t_c]	ln	Gaussian distribution	Flooding hazard [%]
k_s = 1.29 cm				
1	31.21	3.441	0.637	36.2
2	30.10	3.404	0.544	45.5
3	31.45	3.448	0.447	55.3
4	116.96	4.762	0.999	2.2E-05
5	25.53	3.240	0.348	65.2
6	29.61	3.388	0.608	39.1
7	68.49	4.227	0.999	0.05
8	43.52	3.773	0.951	4.8
9	41.98	3.737	0.923	7.6
k_s = 1.98 cm				
1	31.27	3.443	0.620	37.9
2	30.12	3.405	0.522	47.7
3	31.47	3.449	0.420	57.9
4	117.22	4.764	0.999	2.3E-05
5	25.51	3.239	0.326	67.3
6	29.68	3.390	0.592	40.8
7	68.59	4.228	0.999	0.06
8	43.41	3.771	0.947	5.3
9	41.96	3.737	0.917	8.2
k_s = 4.45 cm				
1	31.26	3.442	0.578	42.2
2	30.12	3.405	0.475	52.5
3	31.46	3.449	0.364	63.6
4	117.00	4.762	0.999	2.5E-05
5	25.52	3.239	0.283	71.6
6	29.67	3.390	0.551	44.9
7	68.47	4.226	0.999	0.07
8	43.51	3.773	0.939	6.1
9	41.95	3.736	0.903	9.7
k_s = 5.17 cm				
1	31.27	3.443	0.569	43.0
2	30.15	3.406	0.466	53.4
3	31.45	3.448	0.352	64.7
4	117.24	4.764	0.999	2.5E-05
5	25.50	3.239	0.275	72.5
6	29.64	3.389	0.542	45.8
7	68.60	4.228	0.999	0.07
8	43.44	3.771	0.936	6.3
9	41.93	3.736	0.899	10.0

specifically, for the detailed monitoring of the hydro-geomorphological variables, which are essential to assess future instability scenarios.

Declaration of competing interest

The authors declare that they have no known competing financial interests or personal relationships that could have appeared to influence the work reported in this paper.

Acknowledgements

The activities described in the paper are part of the objectives of the PhD project in Geosciences "Application of UAV system and SfM techniques to address the hydro-geomorphological hazard in a fluvial system" at the Department of Earth and Geoenvironmental Sciences of Bari (Italy) and of the "RPASinAir – Integrazione dei Sistemi Aeromobili a Pilotaggio Remoto nello spazio aereo non segregato per servizi", PON ricerca e innovazione 2014-2020.

References

Aberle, J., Smart, G.M., 2003. The influence of roughness structure on flow resistance on steep slopes. J. Hydraul. Res. 41 (3), 259–269.

Ahamed, A., Bolten, J., Doyle, C., Fayne, J., 2017. Near real-time flood monitoring and impact assessment systems. Remote Sensing of Hydrological Extremes. Springer, Cham, pp. 105–118.

Annis, A., Nardi, F., Petroselli, A., Apollonio, C., Arcangeletti, E., Tauro, F., Grimaldi, S., 2020. UAV-DEMs for small-scale flood hazard mapping. Water 12 (6), 1717.

ASCE, 1992. Design and Construction of Urban Stormwater Management Systems. American Society of Civil Engirneers, New York, NY.

Avand, M., Kuriqi, A., Khazaei, M., Ghorbanzadeh, O., 2022. DEM resolution effects on machine learning performance for flood probability mapping. J. Hydro Environ. Res. 40, 1–16.

Bates, P.D., Marks, K.J., Horritt, M.S., 2003. Optimal use of high-resolution topographic data in flood inundation models. Hydrol. Process. 17 (3), 537–557.

Biron, P.M., Choné, G., Buffin-Bélanger, T., Demers, S., Olsen, T., 2013. Improvement of streams hydro-geomorphological assessment using LiDAR DEMs. Earth Surf. Process. Landf. 38 (15), 1808–1821.

Bizzi, S., Demarchi, L., Grabowski, R.C., et al., 2016. The use of remote sensing to characterise hydromorphological properties of European rivers. Aquat. Sci. 78, 57–70. https://doi.org/10.1007/s00027-015-0430-7.

Boulton, S.J., Stokes, M., 2018. Which DEM is best for analyzing fluvial landscape development in mountainous terrains? Geomorphology 310, 168–187.

Butler, J.B., Lane, S.N., Chandler, J.H., 2001. Automated extraction of grain-size data from gravel surfaces using digital image processing. J. Hydraul. Res. 39, 519–529. https://doi.org/10.1080/00221686.2001.9628276.

Capolongo, D., Refice, A., Bocchiola, D., D'addabbo, A., Vouvalidis, K., Soncini, A., Stamatopoulos, L., 2019. Coupling multitemporal remote sensing with geomorphology and hydrological modeling for post flood recovery in the Strymonas dammed river basin (Greece). Sci. Total Environ. 651, 1958–1968. https://doi.org/10.1016/j.scitotenv.2018.10.114.

Carrivick, J.L., Smith, M.W., 2019. Fluvial and aquatic applications of structure from motion photogrammetry and unmanned aerial vehicle/drone technology. Wiley Interdiscip. Rev. Water 6 (1), e1328.

Casas, A., Benito, G., Thorndycraft, V.R., Rico, M., 2006. The topographic data source of digital terrain models as a key element in the accuracy of hydraulic flood modelling. Earth Surf. Process. Landforms 31 (4), 444–456.

Davies, L., Bolam, R.C., Vagapov, Y., Anuchin, A., 2018. Review of unmanned aircraft system technologies to enable beyond visual line of sight (BVLOS) operations. 2018 X International Conference on Electrical Power Drive Systems (ICEPDS). IEEE, pp. 1–6.

De Musso, N.M., Capolongo, D., Refice, A., Lovergine, F.P., D'Addabbo, A., Pennetta, L., 2018. Spatial evolution of the december 2013 metaponto plain (Basilicata, Italy) flood event using multi-source and high-resolution remotely sensed data. J. Maps 14 (2), 219–229.

De Musso, N.M., Capolongo, D., Caldara, M., Surian, N., Pennetta, L., 2020. Channel changes and controlling factors over the past 150 years in the Basento River (Southern Italy). Water 12 (1), 307.

Detert, M., Weitbrecht, V., 2012. Automatic object detection to ana- lyze the geometry of gravel grains – a free stand-alone tool. River Flow 2012: Proceedings of the International Conference on Fluvial Hydraulics, San José, Costa Rica, 5–7 September 2012. Taylor & Francis Group, London, UK, pp. 595–600.

Eltner, A., Sofia, G., 2020. Structure from motion photogrammetric technique. Developments in Earth Surface Processes. 23. Elsevier, pp. 1–24.

Endreny, T.A., Wood, E.F., Lettenmaier, D.P., 2000. Satellite-derived digital elevation model accuracy: hydrogeomorphological analysis requirements. Hydrol. Process. 14 (1), 1–20.

Fang, S.X., O'Young, S., Rolland, L., 2018. Development of small uas beyond-visual-line-of-sight (bvlos) flight operations: system requirements and procedures. Drones 2 (2), 13.

Fanta-Jende, P., Steininger, D., Bruckmüller, F., Sulzbachner, C., 2020. A versatile uav near real-time mapping solution for disaster response–concept, ideas and implementation. Int. Arch. Photogramm. Remote. Sens. Spat. Inf. Sci. 43, 429–435.

Farooq, M., Shafique, M., Khattak, M.S., 2019. Flood hazard assessment and mapping of river swat using HEC-RAS 2D model and high-resolution 12-m TanDEM-X DEM (WorldDEM). Nat. Hazards 97 (2), 477–492.

Fonstad, M.A., Dietrich, J.T., Courville, B.C., Jensen, J.L., Carbonneau, P.E., 2013. Topographic structure from motion: a new development in photogrammetric measurement. Earth Surf. Process. Landf. 38 (4), 421–430. https://doi.org/10.1002/esp.3366.

Graham, D.J., Reid, I., Rice, S.P., 2005a. Automated sizing of coarse- grained sediments: image-processing procedures. Math. Geol. 37, 1–28. https://doi.org/10.1007/s11004-005-8745-x.

Hemmelder, S., Marra, W., Markies, H., De Jong, S.M., 2018. Monitoring river morphology & bank erosion using UAV imagery–a case study of the river Buëch, Hautes-Alpes, France. Int. J. Appl. Earth Obs. Geoinf. 73, 428–437.

Horritt, M.S., Bates, P.D., 2001. Effects of spatial resolution on a raster based model of flood flow. J. Hydrol. 253 (1–4), 239–249.

Jain, K.P., Tang, J., Sreenath, K., Mueller, M.W., 2020. Staging energy sources to extend flight time of a multirotor UAV. 2020 IEEE/RSJ International Conference on Intelligent Robots and Systems (IROS. IEEE, pp. 1132–1139.

Jung, S., Jo, Y., Kim, Y.J., 2019. Flight time estimation for continuous surveillance missions using a multirotor UAV. Energies 12 (5), 867.

Karamuz, E., Romanowicz, R.J., Doroszkiewicz, J., 2020. The use of unmanned aerial vehicles in flood hazard assessment. J. Flood Risk Manag. 13 (4), e12622.

Kim, J.S., Lee, C.J., Kim, W., Kim, Y.J., 2010. Roughness coefficient and its uncertainty in gravel-bed river. Water Sci. Eng. 3 (2), 217–232.

Klein, L., Clayton, S., Alldredge, J., Goodwin, P., 2007. Long-term monitoring and evaluation of the Lower Red River Meadow Restoration Project, Idaho, USA. Restor. Ecol. 15, 223–239.

Koutalakis, P., Tzoraki, O., Gkiatas, G., Zaimes, G.N., 2020. Using UAV to capture and record torrent bed and banks, flood debris, and riparian areas. Drones 4 (4), 77.

Kwak, Y., Park, J., Fukami, K., 2013. Near real-time flood volume estimation from MODIS time-series imagery in the Indus River Basin. IEEE J. Sel. Top. Appl. Earth Observ. Remote Sens. 7 (2), 578–586.

La Salandra, M., Miniello, G., Nicotri, S., Italiano, A., Donvito, G., Maggi, G., Dellino, P., Capolongo, D., 2021. Generating UAV high-resolution topographic data within a FOSS photogrammetric workflow using high-performance computing clusters. Int. J. Appl. Earth Obs. Geoinf. 105, 102600. https://doi.org/10.1016/j.jag.2021.102600.

Lau, T.W., Afshar, N.R., 2013. Effect of roughness on discharge. J. Civ. Eng. Sci. Technol. 4 (3), 29–33.

Leopold, L.B., Wolman, M.G., Miller, J.P., 1964. Fluvial Processes in Geomorphology 522 San Francisco.

Mancini, F., Dubbini, M., Gattelli, M., Stecchi, F., Fabbri, S., Gabbianelli, G., 2013. Using unmanned aerial vehicles (UAV) for high-resolution reconstruction of topography: the structure from motion approach on coastal environments. Remote Sens. 5, 6880–6898. https://doi.org/10.3390/rs5126880.

Manfreda, S., Di Leo, M., Sole, A., 2011. Detection of flood-prone areas using digital elevation models. J. Hydrol. Eng. 16 (10), 781–790.

Manfreda, S., McCabe, M.F., Miller, P.E., Lucas, R., Pajuelo Madrigal, V., Mallinis, G., Toth, B., 2018. On the use of unmanned aerial systems for environmental monitoring. Remote Sens. 10 (4), 641.

Marteau, B., Vericat, D., Gibbins, C., Batalla, R.J., Green, D.R., 2017. Application of structure-from-motion photogrammetry to river restoration. Earth Surf. Process. Landf. 42 (3), 503–515.

Md Ali, A., Solomatine, D.P., Di Baldassarre, G., 2015. Assessing the impact of different sources of topographic data on 1-D hydraulic modelling of floods. Hydrol. Earth Syst. Sci. 19 (1), 631–643.

Medici, L., Bellanova, J., Belviso, C., Cavalcante, F., Lettino, A., Ragone, P.P., Fiore, S., 2011. Trace metals speciation in sediments of the Basento River (Italy). Appl. Clay Sci. 53 (3), 414–442.

Micheletti, N., Chandler, J.H., Lane, S.N., 2015. Structure from motion (SFM) photogrammetry. ISSN: 2047-0371, Chap. 2, Sec. 2.2In: Clarke, L.E., Nield, J.M. (Eds.), Geomorphological Techniques, Online edition British Society for Geomorphology, London . https://hdl.handle.net/2134/17493.

Neal, J., Schumann, G., Bates, P., Buytaert, W., Matgen, P., Pappenberger, F., 2009. A data assimilation approach to discharge estimation from space. Hydrol. Process. 3649, 3641–3649.

Niethammer, U., James, M.R., Rothmund, S., Travelletti, J., Joswig, M., 2012. UAV-based remote sensing of the Super-Sauze landslide: evaluation and results. Eng. Geol. 128, 2–11.

Ogania, J.L., Puno, G.R., Alivio, M.B.T., Taylaran, J.M.G., 2019. Effect of digital elevation model's resolution in producing flood hazard maps. Glob. J. Environ. Sci. Manag. 5 (1), 95–106.

Papaioannou, G., Loukas, A., Vasiliades, L., Aronica, G.T., 2016. Flood inundation mapping sensitivity to riverine spatial resolution and modelling approach. Nat. Hazards 83 (1), 117–132.

Piccarreta, M., Capolongo, D., Miccoli, M.N., 2012. Deep gullies entrenchment in valley fills during the Late Holocene in the Basento basin, Basilicata (southern Italy). Géomorphologie 18 (2), 239–248.

Piccarreta, M., Pasini, A., Capolongo, D., Lazzari, M., 2013. Changes in daily precipitation extremes in the Mediterranean from 1951 to 2010: the Basilicata region, southern Italy. Int. J. Climatol. 33 (15), 3229–3248.

Podhorányi, M., Unucka, J., Bobál', P., Říhová, V., 2013. Effects of LIDAR DEM resolution in hydrodynamic modelling: model sensitivity for cross-sections. Int. J. Digit. Earth 6 (1), 3–27.

Rinaldi, M., Surian, N., Comiti, F., Bussettini, M., 2016. IDRAIM–Sistema di valutazione idromorfologica, analisi e monitoraggio dei corsi d'acqua. Versione aggiornata 2016–ISPRA–Manuali e Linee Guida 131/2016. Roma, gennaio 400 pp.

Rinaldi, M., Belletti, B., Bussettini, M., Comiti, F., Golfieri, B., Lastoria, B., Surian, N., 2017. New tools for the hydromorphological assessment and monitoring of European streams. J. Environ. Manag. 202, 363–378.

Rusnák, M., Sládek, J., Kidová, A., Lehotský, M., 2018. Template for high-resolution river landscape mapping using UAV technology. Measurement 115, 139–151.
Saksena, S., Merwade, V., 2015. Incorporating the effect of DEM resolution and accuracy for improved flood inundation mapping. J. Hydrol. 530, 180–194.
Scheidegger, A.E., 1973. Hydrogeomorphology. J. Hydrol. 20 (3), 193–215.
Schindelin, J., Arganda-Carreras, I., Frise, E., et al., 2012. Fiji: an open-source platform for biological-image analysis. Nature Methods 9, 676–682. https://doi.org/10.1038/nmeth.2019.
Schlichting, H., Gersten, K., 2016. Boundary-layer theory. Springer.
Tamminga, A.D., Eaton, B.C., Hugenholtz, C.H., 2015. UAS-based remote sensing of fluvial change following an extreme flood event. Earth Surf. Process. Landf. 40 (11), 1464–1476.
Thumser, P., Kuzovlev, V.V., Zhenikov, K.Y., Zhenikov, Y.N., Boschi, M., Boschi, P., Schletterer, M., 2017. Using structure from motion (sfm) technique for the characterisation of riverine systems - case study in the headwaters of the volga river. Geogr. Environ. Sustain. 10 (3), 31–43. https://doi.org/10.24057/2071-9388-2017-10-3-31-43.
Vaughan, I.P., Diamond, M., Gurnell, A.M., Hall, K.A., Jenkins, A., Milner, N.J., Ormerod, S.J., 2009. Integrating ecology with hydromorphology: a priority for river science and management. Aquat. Conserv. Mar. Freshwat. Ecosyst. 19 (1), 113–125.
von Kármán, T., 1930. Mechanische Ähnlichkeit und Turbulenz. Nachrichten von der Gesellschaft der Wissenschaften zu Göttingen, Fachgruppe 1 (Mathematik). 5, pp. 58–76 (also as: “Mechanical Similitude and Turbulence”, Tech. Mem. NACA, no. 611, 1931).
Wentworth, C., 1922. A scale of grade and class terms for clastic sediments. Retrieved June 29, 2021, fromJ. Geol. 30 (5), 377–392. http://www.jstor.org/stable/30063207.
Westoby, M.J., Brasington, J., Glasser, N.F., Hambrey, M.J., Reynolds, J.M., 2012. Structure-from-Motion’photogrammetry: a low-cost, effective tool for geoscience applications. Geomorphology 179, 300–314.
Wheaton, J., Brasington, J., Darby, S., Sear, D.A., 2010. Accounting for uncertainty in DEMs from repeat topographic surveys: improved sediment budgets. Earth Surf. Process. Landf. 35, 136–156.
Williams, R., 2012. DEMs of difference. Geomorphol. Techniques 2 (3.2).
Woodget, A.S., Austrums, R., 2017. Subaerial gravel size measurement using topographic data derived from a UAV-SfM approach. Earth Surf. Process. Landf. 42 (9), 1434–1443. https://doi.org/10.1002/esp.4139.
Woodget, A.S., Fyffe, C., Carbonneau, P.E., 2018. From manned to unmanned aircraft: adapting airborne particle size mapping methodologies to the characteristics of sUAS and SfM. Earth Surf. Process. Landf. 43 (4), 857–870.